crystals

MDPI

Article

Excellent Double-Aging Strengthening Effect with the High Density γ′ Phase of 945A Nickel-Based Alloy

Haiding Liu [1,2], Dongzhe Wang [3,4], Lingping Zhou [1,*], Jia She [5,*], Peng Peng [6,*], Qubo He [2,3] and Wei Wu [2,3]

1 College of Materials Science and Engineering, Hunan University, Changsha 410082, China; liuhaiding@cmri.cc
2 Chongqing Materials Research Institute Co., Ltd. (CMRI), Chongqing 400707, China; qubohe@aliyun.com (Q.H.); ww_ui@163.com (W.W.)
3 Chongqing Key Laboratory of Corrosion-Resistant Alloys, Chongqing 400707, China; wwwwdz@sina.com
4 National Engineering Research Center for Instrument Functional Materials, Chongqing 400707, China
5 College of Materials Science and Engineering, Chongqing University, Chongqing 400044, China
6 School of Metallurgy and Material Engineering, Chongqing University of Science and Technology, Chongqing 401331, China
* Correspondence: lpzhou@hnu.edu.cn (L.Z.); jiashe@cqu.edu.cn (J.S.); peng_pp@foxmail.com (P.P.)

Abstract: The double-aging strengthening effect of the γ′ phase in 945A nickel-based alloy was investigated. The double-aging treatment significantly improved the compressive yield stress. The sample after 8 h aging at 725 °C and 96 h at 800 °C exhibited the highest compressive yield stress of 1007 MPa, which greatly exceeded the original state of 229 MPa. The strengthening mechanism is mainly attributed to the Orowan strengthening mechanism. After double-aging treatment, high density γ′ phase precipitate was formed, which effectively improves the strength. The precipitate behavior and the strengthening mechanism of γ′ phase precipitates were clarified in detail.

Keywords: 945A Ni-based alloy; double-aging; Orowan strengthening

Citation: Liu, H.; Wang, D.; Zhou, L.; She, J.; Peng, P.; He, Q.; Wu, W. Excellent Double-Aging Strengthening Effect with the High Density γ′ Phase of 945A Nickel-Based Alloy. *Crystals* **2022**, *12*, 175. https://doi.org/10.3390/cryst12020175

Academic Editors: Berthod Patrice and Helmut Cölfen

Received: 27 October 2021
Accepted: 17 January 2022
Published: 26 January 2022

1. Introduction

Nickel-based (Ni-based) alloys have attracted much attention due to their excellent oxidation resistance, corrosion resistance and mechanical properties under high temperature, and are successfully applied in aero-engine blades, turbine discs, and combustion chambers [1–5]. Such excellent performance of Ni-based alloys originates from the precipitation at high temperatures (600–800 °C). The precipitations contain the γ′ and γ″ phases, which possess $L1_2$ and DO_{22} crystal structures, respectively [6,7].

According to previous research [8–11], the precipitation of the γ′ phase is stable and enhances the mechanical properties. Li et al. [8] investigated the effect of the solution cooling rate on the microstructure evolution and mechanical properties of Ni-based alloy ATI 718Plus. As the solution cooling rate was reduced, the volume fraction of the primary γ′ phase significantly increased, and thus improved the tensile strength and micro-hardness. Saleem et al. [9] reported the aging behavior of the γ′ phase in the Ni-based alloys 954 and 945X. After aging treatment, γ′ phase precipitates with mean diameters of ~7 and ~10 nm were formed, and thus improved the tensile strength to 1100 MPa. The formation of nano-scale precipitates after the aging process significantly improves the mechanical property of Ni-based alloys. Therefore, the precipitation strengthening of the γ′ phase plays an important role in optimizing the mechanical properties of Ni-based alloy. Regulating the γ′ phase by aging treatment is expected to further improve the properties of Ni-based alloy.

For 945A Ni-based alloy, the alloying element content is higher than that of the traditional 718 Ni-based alloy; the values are 53 wt.% and 47 wt.%, respectively [7]. The higher alloying element contents of 945A Ni-based alloy yields better mechanical properties, such as strength, ductility, and resistance to stress corrosion cracking. In addition, the higher alloying element content is beneficial to the aging strengthening. Double-aging

treatment is widely used in other materials and yields a good precipitation strengthening effect [12–14]. In addition, the application fields of Ni-based alloys are usually accompanied by temperature changes, which also make the study of the effect of the double-aging on Ni-based alloys more meaningful [15–17].

In this paper, a double-aging treatment applied to the newly developed 945A Ni-based alloy was carried out. The variation in the microstructure evolution and mechanical properties were investigated. The precipitate behavior and the strengthening mechanism of γ' phase precipitates were clarified in detail.

2. Materials and Methods

The newly developed 945A Ni-based alloy was composed of Fe, Cr, Nb, Mo, Cu, Ti, Mn, and Al, and other impure elements. The ingot was fabricated by the vacuum induction melting plus electroslag remelting duplex smelting process. The size of the as-cast ingot was 160 mm in diameter and 100 mm in height. An X-ray fluorescence spectrometer (XRF, 800CCDE, Shimadzu Corporation, Shimadzu, Japan) was employed to detect the chemical composition of the ingot. The result is shown in Table 1. After the casting process, the ingot was deformed to a bar having a diameter of 16 mm by the plastic processes, which were combined with forging and rolling. The beginning temperature of the forging process was 1160 °C, and the finished temperature was 950 °C. After forging, the ingot was formed into a cuboid having a cross-section size of 40 mm × 40 mm. The following rolling process was also conducted at 1160 °C, and finished at 950 °C. After rolling, a bar having a diameter of 16 mm was obtained. To achieve a good aging effect, the bar was homogenized at 1060 °C for 1 h and then water quenched.

Table 1. The chemical composition of the 945A Ni-based alloy.

Alloy	Fe	Cr	Nb	Mo	Cu	Ti	Mn	Al	Other	Ni
945A Ni-based alloy	18.3	21.7	4.0	3.6	1.8	1.0	0.5	0.5	0.3	48.3

The double-aging treatment of the fabricated bar was performed in a resistance furnace. The schematic diagram of the double-aging treatment is shown in Figure 1. Samples were heated to 725 °C, and then aged for 8 h. After the first aging, the temperature was increased to 800 °C. To investigate the effect of double-aging treatment on the 945A Ni-based alloy, the samples were aged at 800 °C for various times. The related parameters are listed in the Table 2. The samples held for 6, 12, 24, 48, and 96 h are denoted as 1#, 2#, 3#, 4#, and 5#, respectively.

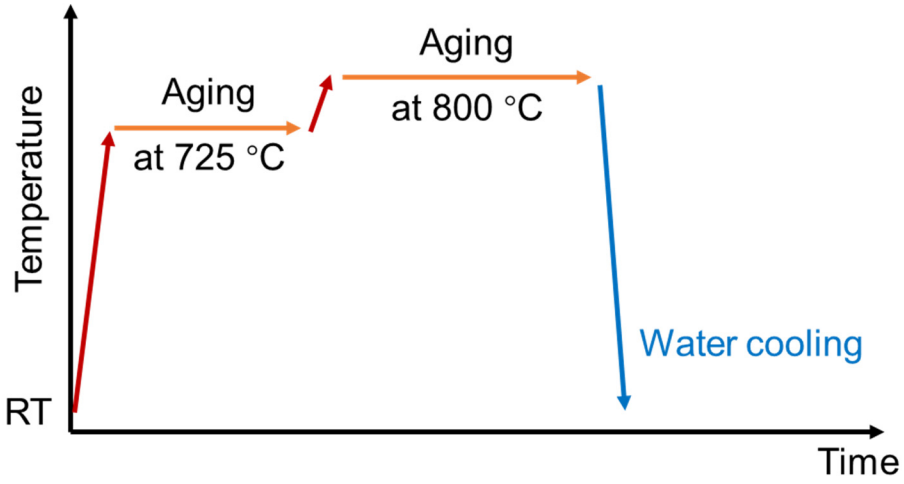

Figure 1. Schematic diagram of the double-aging treatment on the 945A Ni-based alloy.

Table 2. Parameters of the double-aging treatment on the 945A Ni-based alloy.

Sample Number	Double-Aging Parameters	
	First	Second
0#	None	None
1#	725 °C for 8 h	800 °C for 6 h
2#		800 °C for 12 h
3#		800 °C for 24 h
4#		800 °C for 48 h
5#		800 °C for 96 h

The microstructures of the 945A Ni-based alloy were analyzed by transmission electron microscopy (TEM, Philips TECNAI 20, Santa Clara, CA, USA). Samples for TEM testing were mechanical polished using SiC paper to 50 μm, and then thinned using an argon ion thinning machine (PIPS II 695, Gatan, Pleasanton, CA, USA). To identify the precipitates, the High-Angle Annular Dark Field Scan TEM (HAADF-STEM), Energy Dispersive Spectroscopy (EDS) mapping, and Selected Area Diffraction (SAD) were adopted. The acceleration voltage of the TEM test was 200 kV. The related high-resolution TEM (HR-TEM) data and geometric phase analysis (GPA) were conducted on the Digital Micrograph software (DM, Version 3, Ganta, PA, USA). The mechanical properties were evaluated by the compressive test. The tests were performed on the CMT6305-300KN electronic universal testing machine (Skyan power equipment Ltd., Shenzhen, China) at room temperature. The sample size was 6 mm in diameter and 9 mm in height. The test strain rate was 1×10^{-3}, and the samples for each double-aging condition were tested three times to ensure accuracy.

3. Results

Figure 2 shows the bright-field images of the wrought 945A Ni-based alloy after homogenization treatment. A few second phase particles can be observed on the matrix as shown in Figure 2a. From the magnified image of Figure 2b, the particle takes on a lumpy form. This second phase cannot dissolve into the matrix at a high temperature of 1160 °C, which indicates that this second phase is a high temperature stable phase. In Ni-based alloys, such a second phase is generally considered to be a kind of carbide [18]. In addition, many dislocations were observed in the matrix as shown in Figure 2c. These residual dislocations are supposed to be beneficial to the following aging treatment, in which precipitates tend to occur at defects [19,20].

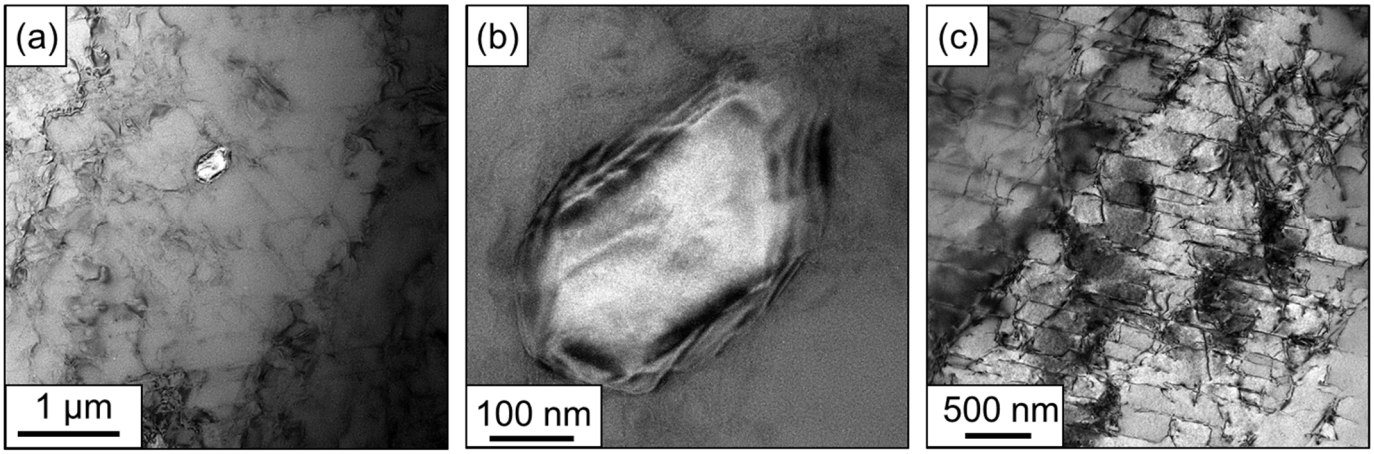

Figure 2. Bright-field images of the wrought 945A Ni-based alloy: (**a**) morphology of low magnification, (**b**) high magnification of the second phase in (**a**), (**c**) the residual dislocations.

To further identify the undissolved particles, HAADF-STEM and EDS mapping were performed on the 945A Ni-based alloy after homogenization treatment. The results are shown in Figure 3. The particles are concentrated by the Ti, Nb, and C elements, which confirm that the particles are carbides. According to the literature [3,4], these carbides in the Ni-based alloy usually contain Ti, Nb, Ta, and V elements, denoted as MC type compounds. Combining Figures 1 and 2, only the carbides can be observed in the matrix, indicating that there was no precipitation behavior before aging treatment.

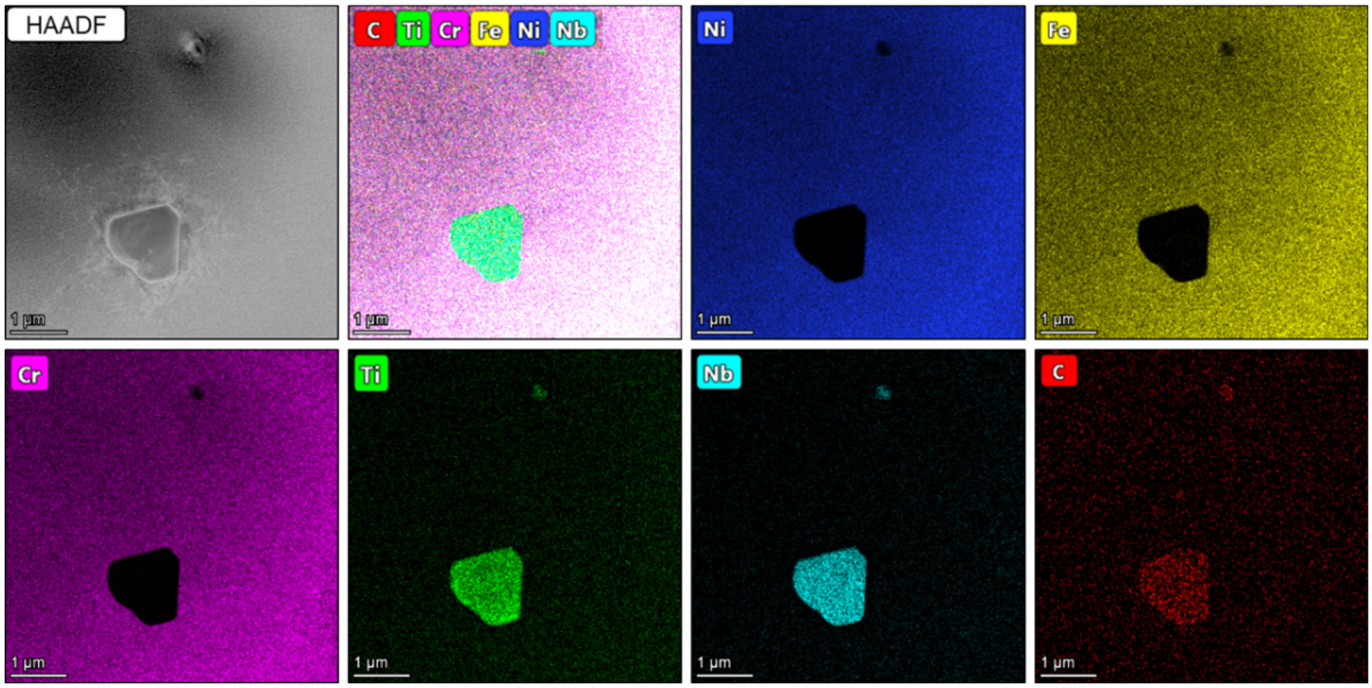

Figure 3. HAADF-STM image of the 945A Ni-based alloy and the related EDS mapping results, the first figure is the HAADF image, element distribution image and the independent element distribution images of Ni, Fe, Cr, Ti, Nb and C, respectively.

Figure 4 shows the engineering stress–strain curves and the comparison diagram of compressive yield stress between the presented double-aging samples and previously directed aging samples [21]. From the engineering stress–strain curves in Figure 4a, the compressive yield stress increases with the increment of the double-aging time. Compared with the original state, the compressive yield stress of all the double-aging processed samples is much higher than that of the original sample. From the data comparison, the stress of the double-aging processed samples increases by 778 MPa compared to the original state, whereas the improvement in the compressive yield stress by the double-aging process in this study exceeds that of the previous directed-aging at 725 °C [21], even at the same aging time. The 5# sample presents the best compressive yield stress of 1007 MPa, which is 778 MPa higher than that of the original state.

Figure 5 shows the bright-field and dark-field TEM images of the 5# sample. From the bright-field and dark-field TEM images in Figure 5a,b, a large fraction of precipitates can be observed in the matrix. The magnified image in Figure 5c illustrates that the morphology of the precipitates presents an ellipse. The particle size is about 50 nm, and the size of the interspace between each precipitate is about 20 nm. To determine the orientation relationship between the precipitated phase and the matrix, the SAD result is shown in Figure 5d. From the SAD results, the γ' phase with a face-centered cubic can be identified, in which a = 0.361 nm. The $(13\bar{1})$ plane of the γ' phase is parallel to the $(11\bar{1})$ planes of the matrix.

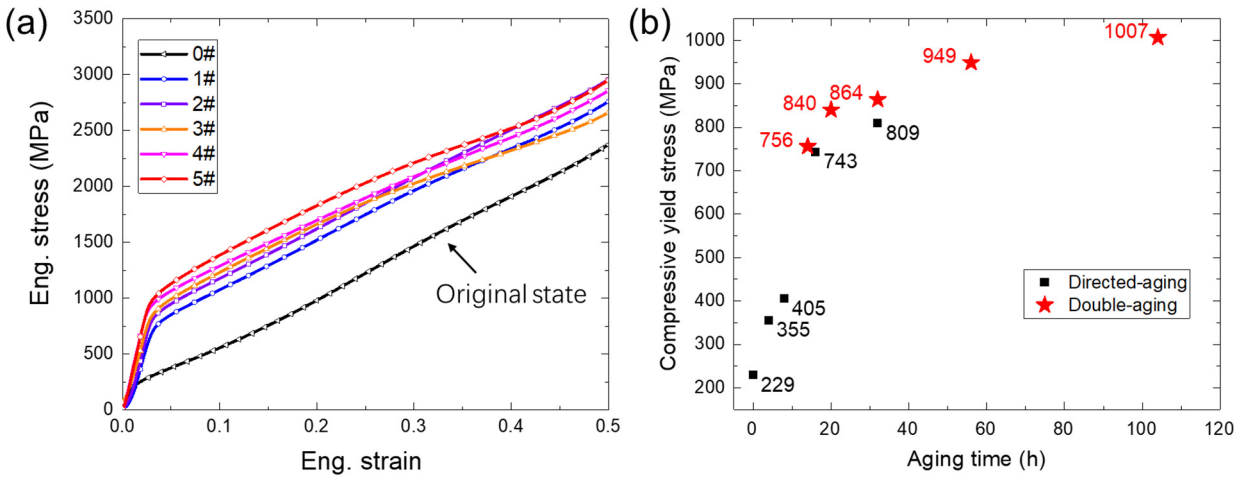

Figure 4. Engineering stress–strain curves of the 945A Ni-based alloys: (**a**) compressive stress–strain curves, (**b**) the compressive yield stress of the presented samples and the previous study of directed aging treatment, data from Ref. [21].

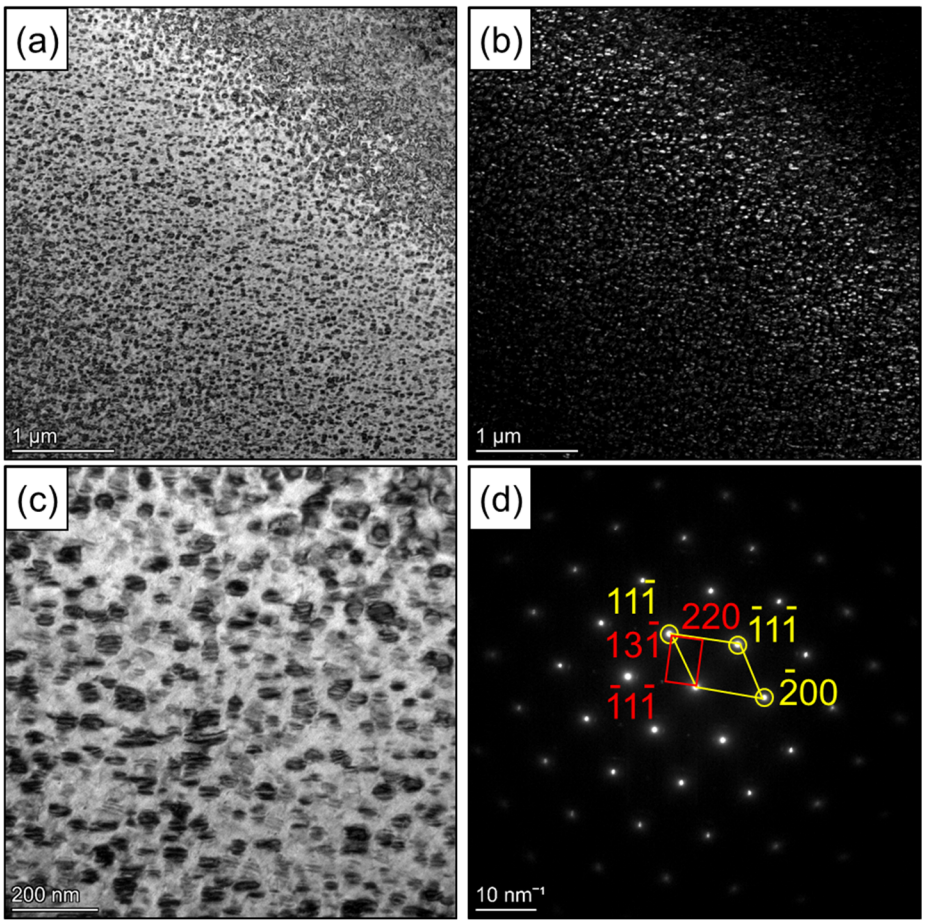

Figure 5. Bright-field and dark-field TEM images of the 5# sample: (**a**) low magnified bright-field image, (**b**) dark-field image, (**c**) high low magnified bright-field image, (**d**) SAD image.

To further identify the chemical composition of the precipitates, HAADF-STEM and EDS mapping analysis were undertaken. The related results of the 5# sample are presented in Figure 6. These precipitates are composed of the Ni, Ti, Nb, and Al elements. According to the literature [22–24], the precipitates in the Ni-based alloy with such alloying elements

are the γ′ phase, which is proved to be Ni_3(Al, Ti, Nb). The large fraction of the γ′ phase enhances the mechanical properties.

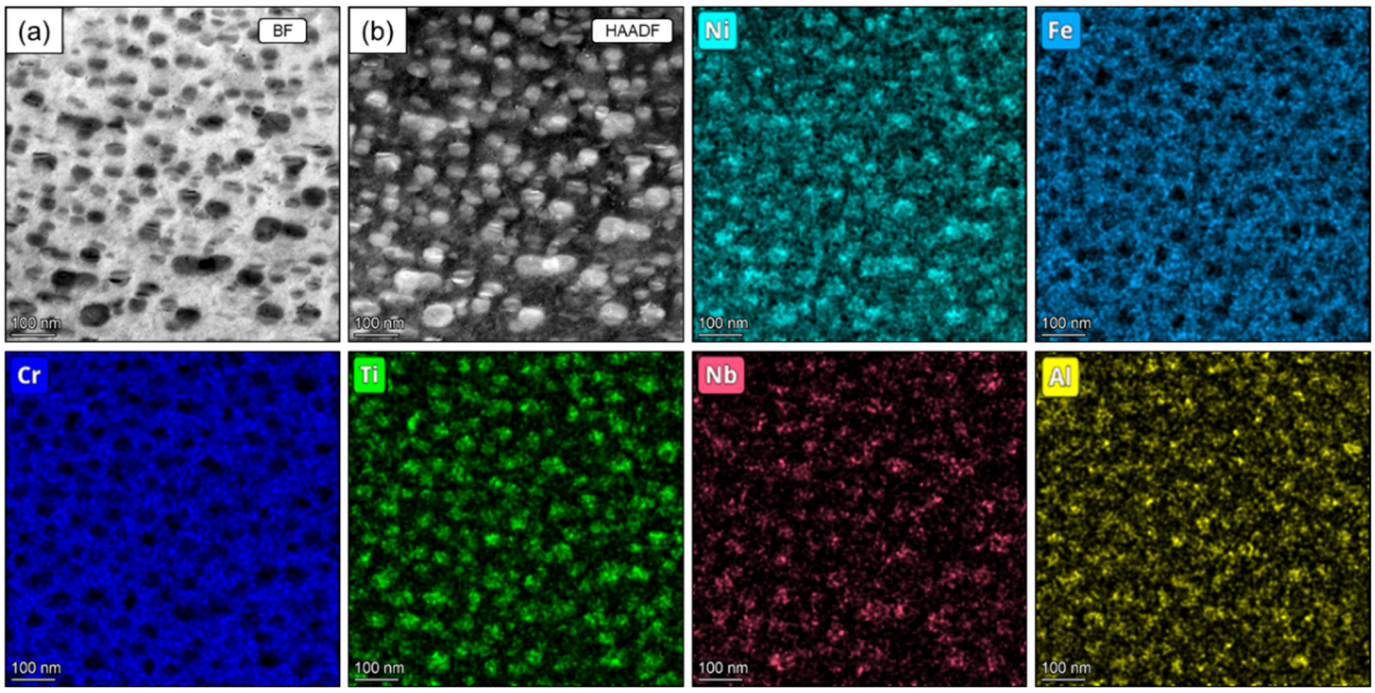

Figure 6. Bright-field, HAADF-STEM image, and the related EDS mapping results of the γ′ phase in the 5# sample: (**a**) the bright-field image, (**b**) HAADF image of (**a**).

4. Discussion

After the double-aging treatment, a large fraction of γ′ phase precipitates is formed. The precipitates can inhibit the dislocation motion during the plastic deformation, and thus enhance the mechanical properties. Therefore, further analysis of the formation of the γ′ phase during the double-aging treatment and the strengthening mechanism is needed.

4.1. γ′ Phase Evolution during the Double-Aging Treatment

The precipitate behavior of the γ′ phase during the double-aging treatment can be divided into two parts. One is the formation of the γ′ phase precipitates in the first aging process, and the other is the particle growth during the second aging process. For the wrought alloys, such as Mg alloy [25,26] and Al alloy [27,28], the precipitates that occur at defects have been widely studied. It has been noted that the atomic segregation tends to occur on the defects, such as dislocation lines, stacking faults, twinning, and sub-grain boundaries [29]. The defect-induced precipitation can promote the effect of aging strengthening. In this work, the dislocations are still maintained after homogenization as shown in Figure 2. These residual dislocations may be the second phase nuclei sites, and the uniform dislocations contribute to the formation of γ′ phase precipitates.

To clarify the formation of the γ′ phase precipitates in the first aging process, the TEM morphology of the γ′ phase precipitates after the first aging process is presented in Figure 7. After aging at 725 °C for 8 h, a large fraction of fine γ′ phase precipitates is formed. From the HRTEM image in Figure 7b, particles having a size of ~8 nm can be found, which exhibit distinct lattice fringes. In addition, under the aging temperature, the solute atoms are supersaturated. According to the spinodal decomposition-like mechanism [30], the supersaturated solid solution spontaneously decomposes into continuous long-range composition fluctuation and forms a new phase of inhomogeneous solid solution. Normally, spinodal decomposition is a process of decreasing free energy. In this process, after the second phase is precipitated, the energy in the system is reduced, making the system reach

the equilibrium state at a certain temperature. The appearance of defects will increase the energy of the system, which can promote the occurrence of spinodal decomposition, and then generate more and faster new phase nuclei.

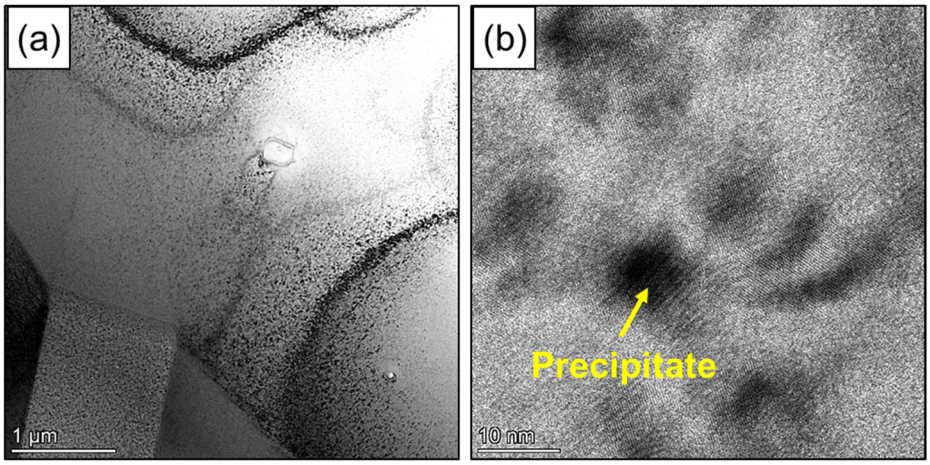

Figure 7. Bright-field TEM and the HRTEM image of the sample after the 725 °C aging treatment: (**a**) bright-field TEM image, (**b**) HRTEM image.

After numerous nucleation of the γ′ phase precipitates, further precipitation and growth of the second phase occur during the following aging treatment. The precipitation and growth of the γ′ phase increases the fraction of the γ′ phase, which can be estimated by the classical JMAKE equation [31]:

$$F_r(t) = 1 - exp(-kt)^n \quad (1)$$

where F_r is the reacted fraction of the γ′ phase, k incorporates the rates of nucleation and growth of the γ′ phase, n is associated with the geometric shape of the γ′ phase, known as the Avrami exponent (which can be a non-integer value), and t is the aging time. In this study, the nuclei rate, the geometric shape, and the aging time of the γ′ phase are the same in the first aging treatment. In the second aging process, the aging time increases. Comparing Figures 5 and 7, the particle size of the first aging is ~8 nm, whereas that of the second aging is ~50 nm. The area fraction of the particles in Figure 5 is 56.3%, whereas it is 14.6% in Figure 7. With the increment in the aging time, the γ′ phase becomes significantly coarser. The coarsening phenomenon remarkably improves the fraction of the γ′ phase in the matrix.

4.2. Strengthening Mechanism of the γ′ Phase

After the double-aging treatment, the fraction of the γ′ phase is improved, which enhances the mechanical properties. Compared with the original state, the improvement in the compressive yield stress of the 5# sample that was double-aged for 96 h was more than 700 MPa, and the compressive yield stress of the 5# sample reached 1007 MPa. This improvement is better than that of direct-aging. The strengthening mechanism can be estimated by the Orowan relationship [32]:

$$\tau_{Orowan} = \left(\frac{Gb}{2\pi\sqrt{1-v}}\right)\left(\frac{1}{\lambda}\right)log\left(\frac{D_p}{r_0}\right) \quad (2)$$

where τ_{Orowan} is the Orowan stress strengthening by the γ′ phase, G is the shear modulus, b is the Burgers vector, v is the Poison ratio, λ is the particle spacing, D_p is the mean planar diameter of the particle, and r_0 is the dislocation core radius. Figure 4 shows that the size of the particle is about 50 nm, and the interspace between each precipitate is about 20 nm. The improvement in the precipitate size and the decrease in the precipitate

interspace increases the Orowan stress strengthening effect. With the increment of the aging time, the compressive yield stress is significantly enhanced. Compared with the previous direct-aging treatment [21], the volume fraction of the γ′ phase is improved, and the interspace between each precipitate is reduced. This enhances the Orowan strengthening effect, which results in higher yield stress. According to the response of the mechanical properties, the yield stresses of the direct-aged sample and double-aged sample are 809 and 864 MPa, respectively. Compared with the original state, the improvement is 580 and 635 MPa, respectively. The double-aged strengthening effect of the Orowan strengthening mechanism of double-aging treatment is better than that of directed aging treatment. Therefore, the samples after double-aging treatment exhibit higher yield stress than that after direct-aging treatment.

In order to intuitively see this Orowan strengthening effect, the TEM observation was undertaken for a 5# sample with 20% compressive strain. The results are shown in Figure 8. From Figure 8a, dislocation walls are clearly observed around the γ′ phase, as marked by the arrows. This suggests that these γ′ phase precipitates can effectively inhibit dislocation motion, forming a large number of black dislocation plug areas. Further magnification of the image to form the HRTEM image is shown in Figure 8b. The Fast Fourier Transform diagram shows that the orientation of the γ′ phase is consistent with that of the results in Figure 5, which illustrates that the $(13\bar{1})$ plane of the precipitates is parallel to the $(11\bar{1})$ planes of the matrix. The matrix lattice distortion near the second phase was analyzed by the GPA method in the DM software. It was found that there are a large number of strain fields in the matrix near the second phase, but there is no strain in the second phase. This indicates a typical dislocation bypass mechanism, also known as the Orowan strengthening mechanism.

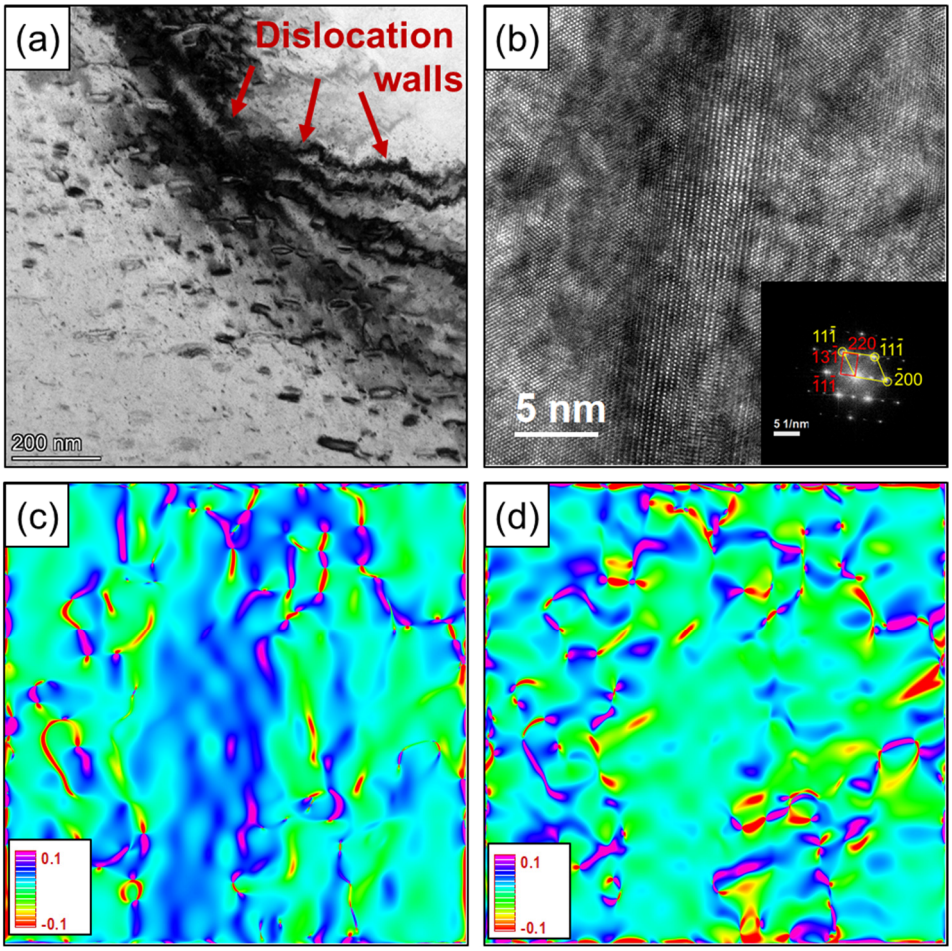

Figure 8. High-resolution TEM image of the 5# sample after compressive tests: (**a**) the interaction between dislocations and the γ′ phase precipitates, (**b**) the high-resolution TEM result, (**c**,**d**) GPA result along the $[11\bar{1}]$ and $[\bar{2}00]$ direction, respectively.

5. Conclusions

This study investigated the effect of double-aging treatments on the 945A Ni-based alloys. The precipitate behavior and the strengthening mechanism of the γ′ phase precipitates were clarified. The main conclusions are listed below:

(1) The double-aging treatment significantly improves the compressive yield stress. The 5# sample exhibits the highest compressive yield stress of 1007 MPa, which exceeded that of the original state of 229 MPa.
(2) With the increment in the double-aging time, the size of the γ′ phase particle improves, and the interspace is reduced. The γ′ phase particle size of the 5# sample is about 50 nm, and the interspace between each precipitate is about 20 nm.
(3) The high density of the γ′ phase is attributed to the formation of many fine γ′ phase nucleation points in the first aging process. In addition, the increased system energy caused by the defects potentially promotes the occurrence of a spinodal decomposition mechanism, which can generate more and faster new phase nuclei.
(4) The strengthening mechanism is mainly attributed to the Orowan strengthening mechanism. After double-aging treatment, a high density of the γ′ phase precipitates occurs, which effectively improves the strength. This strengthening effect of double-aging treatment is better than that of direct aging.

Author Contributions: Conceptualization, H.L. and J.S.; methodology, D.W.; software, D.W.; validation, H.L., D.W., L.Z., J.S. and W.W.; formal analysis, P.P. and J.S.; investigation, H.L.; resources, H.L.; data curation, P.P. and J.S.; writing—original draft preparation, H.L.; —writing, review and editing, H.L., P.P, J.S., Q.H. and L.Z.; visualization, H.L.; supervision, L.Z.; project administration, P.P., Q.H. and J.S.; funding acquisition, L.Z. All authors have read and agreed to the published version of the manuscript.

Funding: This research was funded by the National Key Research and Development Program of China (No. 2021YFB3703000), Major Science and Technology Project of Sinomach [SINOMAST-ZDZX-2018-05].

Institutional Review Board Statement: Not applicable.

Informed Consent Statement: Not applicable.

Data Availability Statement: Not applicable.

Conflicts of Interest: The authors declare no conflict of interest.

References

1. Collins, D.M.; D'Souza, N.; Panwisawas, C.; Papadaki, C.; West, G.D.; Kostka, A.; Kontis, P. Spinodal Decomposition versus Classical γ′ Nucleation in a Nickel-Base Superalloy Powder: An In-Situ Neutron Diffraction and Atomic-Scale Analysis. *Acta Mater.* **2020**, *200*, 959–970. [CrossRef]
2. Ezugwu, E.O.; Wang, Z.M.; Machado, A.R. The Machinability of Nickel-Based Alloys: A Review. *J. Mater. Process. Technol.* **1999**, *86*, 1–16. [CrossRef]
3. Berthod, P.; Lemoine, P.; Aranda, L. Experimental and Thermodynamic Study of Nickel-Based Alloys Containing Chromium Carbides, Part I: Study of the Ni–30 wt% Cr–xC System over the [0–2.0 wt% C] range. *Calphad* **2008**, *32*, 485–491. [CrossRef]
4. Cutler, E.R.; Wasson, A.J.; Fuchs, G.E. Effect of Minor Alloying Additions on the Carbide Morphology in a Single Crystal Ni-Base Superalloy. *Scr. Mater.* **2008**, *58*, 146–149. [CrossRef]
5. Wang, K.; Du, D.; Liu, G.; Pu, Z.; Chang, B.; Ju, J. A Study on the Additive Manufacturing of a High Chromium Nickel-Based Superalloy by Extreme High-Speed Laser Metal Deposition. *Opt. Laser Technol.* **2021**, *133*, 106504. [CrossRef]
6. Lin, Y.C.; Wang, C.Y. Alloying-Element Dependence of Structural, Elastic and Electronic Properties of Nickel-Based Superalloys: Influence of γ′ Volume Fraction. *J. Alloy. Compd.* **2020**, *838*, 155141. [CrossRef]
7. Edtmaier, C.; Wolf, M.; de Oro Calderon, R.; Schubert, W.-D. Effect of Nickel on the Formation of γ/γ′ Microstructures in WC/Co-Ni-Al-W. *Int. J. Refract. Met. Hard Mater.* **2021**, *100*, 105652. [CrossRef]
8. Li, J.; Ding, R.; Guo, Q.; Li, C.; Liu, Y.; Wang, Z.; Li, H.; Liu, C. Effect of Solution Cooling Rate on Microstructure Evolution and Mechanical Properties of Ni-Based Superalloy ATI 718Plus. *Mater. Sci. Eng. A* **2021**, *812*, 141113. [CrossRef]
9. Saleem, B.; Dong, H.B.; Patel, V. Effect of Aging on the Strength of Corrosion-Resistant Incoloy Alloys 945 and 945X: A Microstructural Perspective. *Mater. Sci. Eng. A* **2019**, *748*, 327–336. [CrossRef]
10. Flageolet, B.; Jouiad, M.; Villechaise, P.; Mendez, J. On the Role of γ Particles within γ′ Precipitates on Damage Accumulation in the P/M Nickel-Base Superalloy N18. *Mater. Sci. Eng. A* **2005**, *399*, 199–205. [CrossRef]

11. Vernier, S.; Franchet, J.-M.; Dumont, C.; Vennéguès, P.; Bozzolo, N. γ' Precipitates with a Twin Orientation Relationship to Their Hosting Grain in a γ-γ' Nickel-Based Superalloy. *Scr. Mater.* **2018**, *153*, 10–13. [CrossRef]
12. Kim, I.; Song, M.; Kim, J. Nanocluster Formation and Two-Step Aging Behavior in Al–Mg–Si(-xCu: X = 0–4 mass%) Alloys. *J. Alloy. Compd.* **2021**, *857*, 157596. [CrossRef]
13. Gu, K.; Zeng, X.-Q.; Chen, B.; Wang, Y.-X. Effect of Double Aging on Mechanical Properties and Microstructure of EV31A Alloy. *Trans. Nonferr. Met. Soc. China* **2021**, *31*, 2606–2614. [CrossRef]
14. Nick, M.; Feuerhack, A.; Bergs, T.; Clausmeyer, T. Numerical Investigation of Damage in Single-step, Two-step, and Reverse Deep Drawing of Rotationally Symmetric Cups from DP800 Dual Phase Steel. *Proced. Manuf.* **2020**, *47*, 636–642. [CrossRef]
15. Wu, R.; Zhao, Y.; Yin, Q.; Wang, J.; Ai, X.; Wen, Z. Atomistic Simulation Studies of Ni-Based Superalloys. *J. Alloy. Compd.* **2021**, *855*, 157355. [CrossRef]
16. Xia, W.; Zhao, X.; Yue, L.; Zhang, Z. A Review of Composition Evolution in Ni-Based Single Crystal Superalloys. *J. Mater. Sci. Technol.* **2020**, *44*, 76–95. [CrossRef]
17. Long, H.; Mao, S.; Liu, Y.; Zhang, Z.; Han, X. Microstructural and Compositional Design of Ni-Based Single Crystalline Superalloys—A Review. *J. Alloy. Compd.* **2018**, *743*, 203–220. [CrossRef]
18. Günther, K.; Bergmann, J.P. Understanding the Dissolution Mechanism of Fused Tungsten Carbides in Ni-Based Alloys: An Experimental Approach. *Mater. Lett.* **2018**, *213*, 253–256. [CrossRef]
19. She, J.; Peng, P.; Tang, A.T.; Zhang, J.Y.; Mao, J.J.; Liu, T.T.; Zhou, S.B.; Wang, Y.; Pan, F.S. Novel on-Line Twist Extrusion Process for Bulk Magnesium Alloys. *Mater. Des.* **2019**, *182*, 108011. [CrossRef]
20. She, J.; Zhou, S.B.; Peng, P.; Tang, A.T.; Wang, Y.; Pan, H.C.; Yang, C.L.; Pan, F.S. Improvement of Strength-Ductility Balance by Mn Addition in Mg–Ca Extruded Alloy. *Mater. Sci. Eng. A* **2020**, *772*, 138796. [CrossRef]
21. Liu, H.; Wang, D.; Zhou, L.; She, J.; Wu, W. Significant Improvement of Strength in Wrought 945A Ni-Based Superalloy by Aging Treatment. *Crystals* **2021**, *11*, 627. [CrossRef]
22. Li, F.; Fu, R.; Yin, F.; Feng, D.; Wang, H.; Du, G.; Feng, Y. Impact of γ'(Ni3(Al,Ti)) Phase on Dynamic Recrystallization of a Ni-Based Disk Superalloy during Isothermal Compression. *J. Alloy. Compd.* **2017**, *693*, 1076–1082. [CrossRef]
23. Yamada, T.; Abe, E.; Osawa, C.; Yukawa, N. Prediction on Microstructure and Mechanical Properties of Hot Forged Ni-Based Super Alloy by Optimization Using Genetic Algorithms. *Proced. Manuf.* **2018**, *15*, 356–363. [CrossRef]
24. Robouch, B.V.; Burattini, E.; Kisiel, A.; Suvorov, A.L.; Zaluzhnyi, A.G. Strained-Tetrahedra Statistical Model for Atomic Distances and Site Occupations in Ternary Intermetallic M3(XX′) Structures Ni3(AlFe) Case. *J. Alloy. Compd.* **2003**, *359*, 73–78. [CrossRef]
25. Peng, P.; Zhang, K.; She, J.; Tang, A.; Zhang, J.; Song, K.; Yang, Q.; Pan, F. Role of Second Phases and Grain Boundaries on Dynamic Recrystallization Behavior in ZK60 Magnesium Alloy. *J. Alloy. Compd.* **2020**, *861*, 157958. [CrossRef]
26. Peng, P.; She, J.; Tang, A.; Zhang, J.; Song, K.; Yang, Q.; Pan, F. A Strategy to Regulate the Microstructure and Properties of Mg-2.0Zn-1.5Mn Magnesium Alloy by Tracing the Existence of Mn Element. *J. Alloy. Compd.* **2022**, *890*, 161789. [CrossRef]
27. Langelandsvik, G.; Furu, T.; Reiso, O.; Roven, H.J. Effects of Iron Precipitation and Novel Metal Screw Extrusion on Electrical Conductivity and Properties of AA1370 Aluminium. *Mater. Sci. Eng. B* **2020**, *254*, 114505. [CrossRef]
28. Kim, D.; Kim, J.; Wenner, S.; Thronsen, E.; Marioara, C.D.; Holmestad, R.; Kobayashi, E. Precipitation Behavior of Al-Si-Cu-Mg(-Fe) Alloys by a Deformation-Semisolid Extrusion Process. *Mater. Charact.* **2021**, *173*, 110863. [CrossRef]
29. Charpagne, M.A.; Polonsky, A.T.; Echlin, M.P.; Jacomet, S.; Jaeger, J.d.; De Graef, M.; Bozzolo, N.; Pollock, T.M. Growth Accidents Induced by Primary γ' Precipitates in a Polycrystalline Nickel-Based Superalloy. *Scr. Mater.* **2020**, *186*, 109–113. [CrossRef]
30. Zhou, X.; Darvishi Kamachali, R.; Boyce, B.L.; Clark, B.G.; Raabe, D.; Thompson, G.B. Spinodal Decomposition in Nanocrystalline Alloys. *Acta Mater.* **2021**, *215*, 117054. [CrossRef]
31. Pandolfi, G.S.; Martins, S.C.; Buono, V.T.L.; Santos, L.A. Precipitation Kinetics of Ti3Ni4 and Multistage Martensitic Transformation in an Aged Ni–Rich Ni–Ti Shape Memory Alloy. *J. Mater. Res. Technol.* **2020**, *9*, 9162–9173. [CrossRef]
32. Peng, P.; Tang, A.; Wang, B.; Zhou, S.; She, J.; Zhang, J.; Pan, F. Achieving Superior Combination of Yield Strength and Ductility in Mg–Mn–Al Alloys via Ultrafine Grain Structure. *J. Mater. Res. Technol.* **2021**, *15*, 1252–1265. [CrossRef]